HHS Public Access

Author manuscript

Quant Infrared Thermogr J. Author manuscript; available in PMC 2015 September 30.

Published in final edited form as:

Quant Infrared Thermogr J. 2015 ; 12(2): 173–183. doi:10.1080/17686733.2015.1046677.

Rapid vs. delayed infrared responses after ischemia reveal recruitment of different vascular beds

Ken Chang[a], **Stephen Yoon**[a], **Niral Sheth**[a], **Miles Seidel**[a], **Matthew Antalek**[a], **James Ahad**[a], **Thomas Darlington**[a], **Allison Ikeda**[b], **Gregory J. Kato**[c,d], **Hans Ackerman**[b], and **Alexander M. Gorbach**[a,*]

[a]Infrared Imaging and Thermometry Unit, National Institute of Biomedical Imaging and Bioengineering, National Institutes of Health, Bethesda, MD, USA

[b]The Laboratory of Malaria and Vector Research, National Institute of Allergy and Infectious Diseases, National Institutes of Health, Rockville, MD, USA

[c]The Hematology Branch, National Heart, Lung, and Blood Institute, National Institutes of Health, Bethesda, MD, USA

[d]Division of Hematology/Oncology, Vascular Medicine Institute, University of Pittsburgh Medical Center, Pittsburgh, PA, USA

Abstract

Continuous infrared imaging revealed transient changes in forearm temperature during arterial occlusion, reperfusion, and recovery in a healthy subject group. Processing the imaging data with the *k-means* algorithm further revealed reactive vascular sites in the skin with rapid or delayed temperature amplification. The observed temporal and spatial diversity of blood-flow-derived forearm temperature allow consideration of thermal-imaging guided placement of skin sensors to achieve enhanced sensitivity in monitoring of skin hemodynamics.

Keywords

infrared imaging; post-occlusion reactive hyperemia; angiosome; peripheral vasculature; skin microcirculation; k-means; thermography; image processing; temperature regulation; precision placement of sensors

*Corresponding author. gorbacha@mail.nih.gov.

Disclosure statement

No potential conflict of interest was reported by the authors.

1. Introduction

Although techniques exist to measure micro- and macro-circulation [1] in skin (capillaroscopy, laser Doppler flowmetry [LDF], laser speckle contrast, and photoplethysmography) and within skeletal muscle (Doppler ultrasound), infrared (IR) imaging provides the advantage of being a modality capable of assessing cutaneous and subcutaneous vessels simultaneously. This is because IR imaging captures heat conducted as well as convected to the skin's surface. Other studies have used high resolution IR imaging to assess blood flow in rat kidneys and human brains.[2, 3] A study by Gorbach et al. showed that skin temperature correlated significantly with forearm blood flow in patients with sickle cell anaemia.[4] To assess blood flow dynamics in healthy subjects, the post-occlusive reactive hyperemia (PORH) test, a standard test of circulatory function, was combined with IR imaging of the volar aspect of the forearm. IR measurements were validated through comparison with blood flux measurements using laser Doppler flowmetry probes.

2. Methods

2.1. Study population

The study enrolled 38 healthy volunteers. All subjects gave written, informed consent for an approved National Heart, Lung, and Blood Institute, NIH protocol #12-H-0101. See http://www.clinicaltrials.gov/ct2/show/NCT01568710 for enrollment criteria. Subjects were between 18 and 70 years of age. IR imaging studies from four healthy volunteers were excluded due to excessive arm movement.

2.2. PORH test

Subjects were studied in a temperature-controlled room (21.1 ± 0.9 °C). Temperature fluctuations in the room were recorded continuously with a data logger (Datalogger 42270, Extech Instruments, USA). Each subject was seated in a hospital bed inclined at a 45° angle, with either the left or right hand secured to a padded armrest at heart level with the volar aspect of the forearm facing upward. All subjects were instructed to remain still during imaging, and a Velcro strap was used to minimise involuntary movements. Prior to the PORH test, all subjects were given a 20 min period of acclimatisation to the room. During the test, full occlusion of the left arm was achieved by automated inflation of an upper arm blood pressure cuff (moorVMS-PRES, Moor Instruments, Inc., USA) to at least 60 mm Hg above systolic pressure for 5 min followed by cuff deflation.

2.3. IR imaging

A cooled IR camera (Santa Barbara FocalPlane Array, Lockheed Martin, USA) was positioned 42 cm above the volar aspect of the subject's forearm (Figure 1) and was remotely focused on three triangular thermo-reflective pieces of tape placed on the skin as fiducial markers. For each subject, 5820 IR images (640 × 512 pixels per image) were collected, with each 50 min PORH test consisting of 30 min of baseline, 5 min of occlusion, and 15 min of post-occlusion. IR images were acquired in the 3.0–5.0 μ wavelength range at 1.94 Hz (WinIR software, Lockheed Martin, USA). The camera was able to resolve two

adjacent pixels that differed by 0.015 °C. Temperature calibration was performed prior to imaging as previously described.[4] IR images were displayed in real time, allowing immediate observation of gross changes in arm perfusion. The IR images were then saved as an image cube for subsequent offline analysis.

2.4. Laser Doppler flowmetry

LDF (moorVMS-LDF, Moor Instruments, Inc., USA) was performed on all subjects to measure blood flux concurrently with IR imaging. Three LDF probes were attached to the subject's skin using double-sided sticky O-rings in a line along the medial side of the forearm near the antecubital space, close to the skin area imaged by IR (Figure 1). Skin blood flux values were collected at 40 Hz for each probe using a 785 nm red laser light source during the 50 min PORH test. The flux values were then saved for subsequent offline analysis.

2.5. IR image processing

IR images were processed using MATLAB (R2012b, MathWorks, USA). To reduce motion artefacts, rigid-body image registration was performed by maximising the cross correlation with a chosen reference frame. The IR image intensity units were converted to temperature units (°C) based on a previously stored calibration file.

To define the whole region of interest (ROI_W) for each subject, the volar aspect of the forearm between the wrist and the antecubital space was manually circumscribed on IR images off-line, and time–temperature profiles were calculated for each pixel. To investigate the vascular responses of different territories, the integral of the absolute value of the first derivative within 0–120 s of reperfusion was calculated for each time–temperature profile within the ROI_W, generating an image where each pixel represented the integral value. Following spatial smoothing (4 × 4 pixel moving average), *k-means* (a method to partition pixels into clusters based on the nearest mean [5]) was implemented in the image to classify pixels as either part of the reactive region of interest (ROI_R, pixels with high integral values) or part of the non-reactive region of interest (ROI_{NR}, pixels with low integral values) (Figure 2, Step I). Next, time–temperature profiles were extracted for pixels within the ROI_R. The variance within 0–120 s of reperfusion was calculated for each time–temperature profile, generating an image where each pixel represented the variance value. Following spatial smoothing (4 × 4 pixel moving average), *k-means* clustering was implemented on the resulting image to classify pixels as either part of the early reactive region of interest (ROI_{ER}, pixels with high variance) or part of the late reactive region of interest (ROI_{LR}, pixels with low variance) (Figure 2, Step II).

Detrending and baseline correction procedures (Figure 2, Step III) were implemented to eliminate a cooling trend observed in the IR-derived temperature data. Time–temperature profiles were extracted from the ROI_R, ROI_{ER}, ROI_{LR}, and ROI_{NR} (Figure 3) over the 50 min duration of imaging and were spatially averaged within each ROI. The time–temperature profiles from the ROI_R, ROI_{ER}, and ROI_{LR} were detrended by subtracting the time–temperature profile of the ROI_{NR}, to delineate the temperature response of the reactive regions relative to the nonreactive regions. To account for different cooling trends in the

ROI_R, ROI_{ER}, and ROI_{LR} compared to the ROI_{NR}, baseline correction was applied to the detrended time–temperature profiles of the ROI_R, ROI_{ER}, and ROI_{LR}. Baseline correction consisted of first creating an approximation of the trend by taking a moving average (232 s time window) of the first 26 min of the baseline period and the last 25 s of the study, and by linearly interpolating the time period in between. Each ROI's trend approximation was then subtracted from the corresponding detrended time–temperature profile.

Next, the following time points and temperature values from the detrended, baseline-corrected time–temperature profiles (Figure 4) were identified for the ROI_R, ROI_{ER}, and ROI_{LR} (derived measurements, Table 1):

1. Time point corresponding to the start of occlusion (t_{occ})
2. Time point corresponding to start of reperfusion (t_{rep})
3. Time point corresponding to maximum temperature derivative during reperfusion (tT'_{max})
4. Time point corresponding to the peak reperfusion (tT_{max})
5. Time point at which temperature returns to baseline during recovery (tT_{rbl})
6. Maximum temperature derivative during reperfusion (T'_{max})
7. Temperature corresponding to the peak of reperfusion (T_{max})
8. Temperature corresponding to 30 s after peak of reperfusion (T_{30s})

Finally, to quantify differences in the dynamics of the PORH test, surrogate markers (Table 2) were calculated using derived measurements for each subject (Figure 2, Step IV).

3. Results

3.1. Reactive regions show amplified response to occlusion and ischemia

For the group ($n = 34$) a median of 15.2% of the ROI_W pixels were classified as ROI_R (Figure 5(a)). ROI_R showed a significant amplification in signal-to-baseline during both occlusion and reperfusion, compared to the ROI_W (Figure 5(b)).

The median T_{max} for ROI_W was 0.033 °C while the median T_{max} for the ROI_R was 0.25 °C ($p < 0.01$). The median T_{min} for ROI_W was −0.03 °C while the median T_{min} for the ROI_R was −0.31 °C ($p < 0.01$).

3.2. IR imaging reflects changes in forearm blood flow during PORH test

The PORH test showed a change of IR-derived temperature on all measurements ($n = 34$). IR revealed both temporal (Figure 6(c)) and spatial (Figure 6(d)–(f)) heterogeneity for each subject. A general similarity between the LDF time–flux profile (Figure 6(b)) and time–temperature profile of the ROI_R (Figure 6(c)) was noted for the occlusion, reperfusion, and recovery segments of the PORH test. After occlusion, temperature declined more slowly than the flux. After reperfusion, the peak of the temperature increase occurred later than the peak increase in flux. The time between reperfusion start and the peak LDF response was 11 s (median), while the time between reperfusion start and the peak temperature response

($\Delta t_{tT_{max}-t_{rep}}$) within the ROI_R was 94 s (median, $p < 0.001$). The group median Spearman's correlation coefficient between time–flux and time–temperature profiles was 0.19 ($p < 0.01$).

3.3. IR imaging revealed spatial blood-flow-derived temperature heterogeneity

In general, ROI_{ER} consisted of small isolated regions, while ROI_{LR} were the areas surrounding ROI_{ER} as well as large venous structures (Figure 3). The percentages of ROI_R, ROI_{ER}, and ROI_{LR} pixels within the ROI_W were calculated (Table 3).

3.4. IR imaging revealed temporal blood-flow-derived temperature heterogeneity

For all measurements ($n = 34$), the classification algorithm was capable of separating ROI_R, ROI_{ER}, and ROI_{LR} (Figure 3). Because ROI_{LR} represented a larger proportion of pixels in the ROI_R than ROI_{ER}, the ROI_R temperature response more closely resembled the ROI_{LR} temperature response (Figure 7). The average time differences between the time to T_{max} computed for ROI_{ER} and ROI_{LR} was 53 s (Figure 7(b)–(c)).

Calculated surrogate markers for the ROI_R, ROI_{ER}, and ROI_{LR} are shown in Table 4.

4. Discussion

We used IR imaging to measure skin temperature in 34 healthy subjects during an occlusion–reperfusion manoeuvre. We found that most of the volar surface of the forearm does not change during occlusion-reperfusion, and therefore is not amenable to quantification of the reactive hyperemia. However, by applying a *k-means* partitioning method to identify those areas of the forearm that are thermally reactive, we were able to quantify the reactive hyperemia in terms of magnitude and duration.

The observation of amplified reperfusion responses in multiple areas on the skin surface during occlusion, reperfusion, and recovery (Figure 5) allows speculation about the functional architecture of reactive vasculature in the human forearm. Rapid decrease of the temperature in ROI_R may correspond to the collapse of these vessels during occlusion, and rapid increase of temperature in the same ROI_R may correspond to their recruitment during reperfusion and recovery. The location of ROI_{ER} on IR images may correspond to the projection of terminal arterioles, perforator vessels, and arteriovenous anastomoses on the skin surface. In fact, anastomoses and perforator angiosomes have recently been thermographically identified as part of the human skin angioarchitecture.[6] The location of ROI_{LR} on IR images may correspond to veins connected to arteries and/or arterioles via anastomoses (which have a low-resistance to blood flow during PORH test).[7]

The prolonged temperature response to reperfusion, compared to the more rapid LDF flux response, may be the result of convection of heat from deep (subcutaneous) vascular territories, including both small and large vessels. The observed general similarities between concurrently monitored LDF flux and IR temperature time profiles during the PORH occlusion, reperfusion, and recovery segments support the notion that skin temperature is a surrogate marker for blood flow changes (Figure 6). Furthermore, photoplethysmographic measurement of relative blood volume in the middle finger, following full forearm occlusion on eleven healthy subjects in a previous study, had a maximum response 120 s after

reperfusion start,[6] which is comparable to the $\Delta t_{tT_{max}-t_{rep}}$ of 94 s observed in the ROI_R of the 34 healthy subjects in our study. The study by Stikbakke and Mercer found increases in skin perfusion as measured by LDF with no skin IR temperature changes during reperfusion in the dorsal forearm.[8] They also reported no IR skin temperature changes during arterial occlusion of the forearm. These observations are possibly due to insufficient sensitivity of the IR camera used and/or selection of the dorsal aspect of forearm, which is known to have blood flow lower than the volar aspect.[9] Other reactive hyperemia studies utilising IR and LDF have shown that changes in skin temperature can be observed and are slower and more prolonged than the rapid perfusion changes observed with LDF.[10]

Due to the close relationships among skin temperature and changes in blood flow, IR imaging may serve as a navigational tool for placement of point measurement detectors on areas of the human skin that are most sensitive to vascular perturbation. The observed temporal and spatial heterogeneity of the skin justifies placement of single point detectors [11] over the most reactive vessels, as isolating reactive regions revealed amplified hemodynamic signals. Potentially, this concept of targeted placement of wearable, wireless detectors can be utilised to identify and monitor prognostic indicators of peripheral vascular function in persons afflicted with vascular diseases.

A major strength of our study is that it provides a passive, non-invasive imaging method capable of assessing spatial and temporal heterogeneity of skin blood flow in real time. Secondly, our study was conducted on 34 healthy subjects, which may serve as a reference in studying blood flow in patients with vascular diseases. Third, observed temporal and spatial diversity of blood-flow-derived forearm temperature allows proposing the new concept of using IR imaging for targeted, precision placement of skin sensors for much more sensitive monitoring of skin hemodynamics.

Our study has several limitations as well. The proposed segmentation of forearm vasculature was based on a functional, hemodynamic study. Further studies are required to improve understanding of the anatomical differences between reactive and non-reactive vasculature. Additionally, IR was used in this study solely as a surrogate measure of blood flow, although there may be other physiological factors that influence temperature dynamics of the forearm, such as local inflammation or thermogenic activity of dispersed brown fat. Further studies should look into the effects of these factors.

5. Conclusions

Application of the *k-means* algorithm to the original IR images revealed functional angioarchitecture of subcutaneous vasculature after reperfusion of the human forearm. Specifically, rapid and delayed responses in vascular networks were identified. Variation in occlusion, reperfusion, and recovery for different vascular beds of the forearm might explain the observed temporal and spatial diversity of post-occlusive responses in the subjects studied. These findings may provide a platform for targeted investigation of vascular impairment in other diseases. The observed temporal and spatial diversity of blood flow-derived forearm temperature allow consideration of thermal imaging for precision guidance

of placement of skin sensors to achieve greatly enhanced sensitivity in monitoring of skin hemodynamics.

Acknowledgements

The authors acknowledge the technical contributions of N. Malik, J. Maivelett, J. Meyer, T. Anabere, and L. Mendelsohn, the nursing support of the NIH Clinical Center, and protocol management by M. Hall, S. Housel, and D. Smith. We also acknowledge Dr H. Eden for editing the manuscript. This research was supported by the Intramural Research Programs of the National Heart, Lung, and Blood Institute, the National Institute of Allergy and Infectious Diseases, and the National Institute of Biomedical Imaging and Bioengineering, National Institutes of Health.

References

1. Allen J, Howell K. Microvascular imaging: techniques and opportunities for clinical physiological measurements. Physiol. Meas. 2014; 35:R91–R141. [PubMed: 24910968]
2. Gorbach AM, Wang H, Elster E. Thermal oscillations in rat kidneys: an infrared imaging study. Philos. Trans. R. Soc. A Math. Phys. Eng. Sci. 2008; 366:3633–3647.
3. Gorbach AM, Heiss J, Kufta C, et al. Intraoperative infrared functional imaging of human brain. Ann. Neurol. 2003; 54:297–309. [PubMed: 12953262]
4. Gorbach AM, Ackerman H, Liu W, et al. Infrared imaging of nitric oxide-mediated blood flow in human sickle cell disease. Microvasc. Res. 2012; 84:262–269. [PubMed: 22784510]
5. MacQueen J. Some methods for classification and analysis of multivariate observations. Proc. Fifth Berkeley Symp. Math. Stat. Probab. 1967; 1:281–297.
6. Selvaraj N, Jaryal AK, Santhosh J, et al. Monitoring of reactive hyperemia using photoplethysmographic pulse amplitude and transit time. J. Clin. Monit. Comput. 2009; 23:315–322. [PubMed: 19728121]
7. Archaryya S, Archaryya K. Spontaneous abdominal arteriovenous fistula and polysplenia in a child presenting with brain abscess. BMJ Case Rep. 2013:1–5.
8. Stikbakke E, Mercer JB. An infrared thermographic and laser doppler flowmetric investigation of skin perfusion in the forearm and finger tip following a short period of vascular stasis. Thermology Int. 2008; 18:107–111.
9. Gardner-Medwin JM, Taylor JY, Macdonald IA, et al. An investigation into variability in microvascular skin blood flow and the responses to transdermal delivery of acetylcholine at different sites in the forearm and hand. Br. J. Clin. Pharmacol. 1997; 43:391–397. [PubMed: 9146851]
10. Hanssler L, Hendricks O, Ranft J, et al. Reactive hyperemia after arterial occlusion: comparison of infrared telethermography and laser Doppler flowmetry. Vasa. 1995; 24:148–154. [PubMed: 7793147]
11. Webb RC, Bonifas AP, Behnaz A, et al. Ultrathin conformal devices for precise and continuous thermal characterization of human skin. Nat. Mater. 2013; 12:938–944. [PubMed: 24037122]

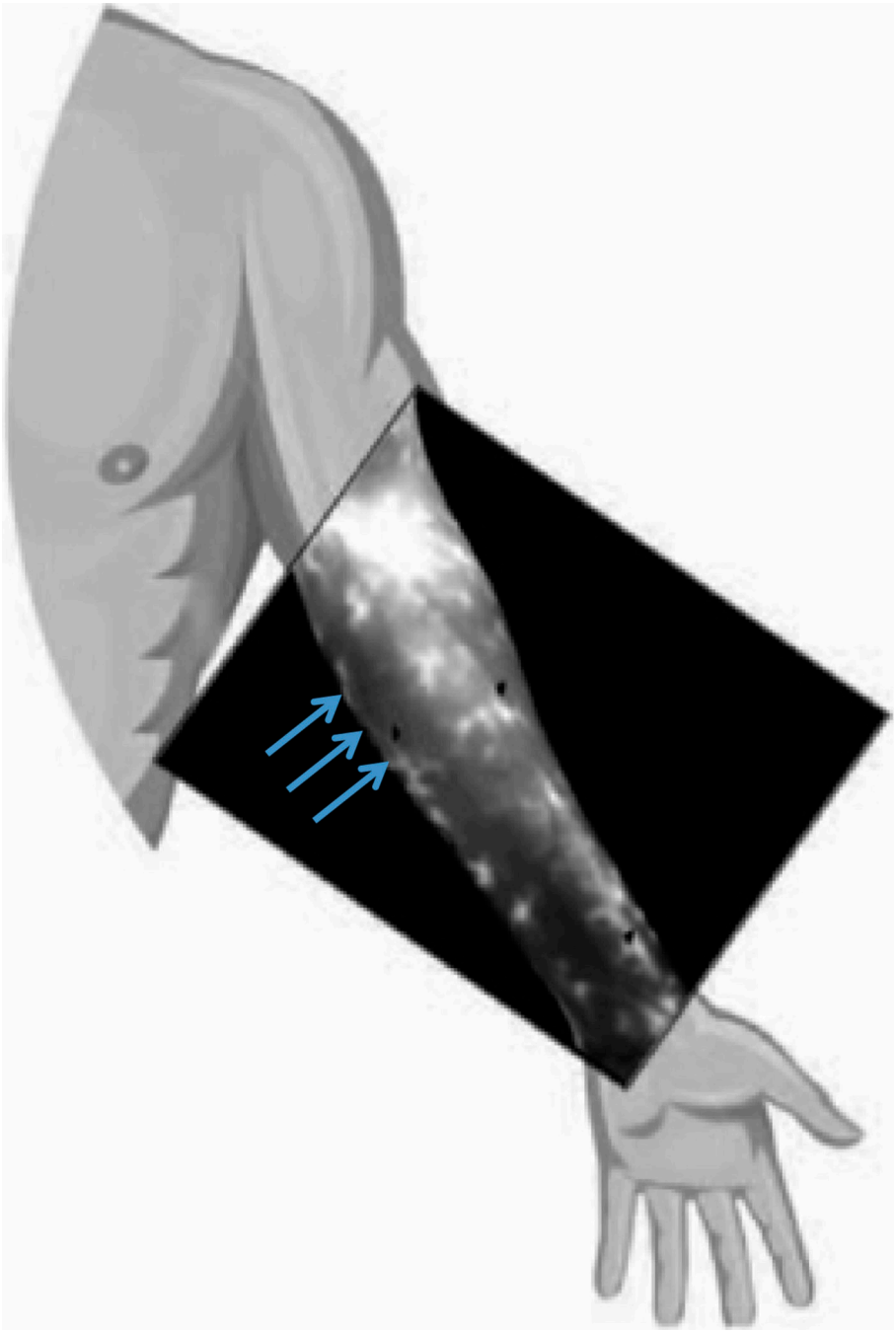

Figure 1.

Representative IR Image overlying cartoon of volar aspect of the left forearm. Notes: Bright areas indicate regions with higher skin temperature, while dark areas indicate regions with lower skin temperature. The fiducial markers (three pieces of thermo-reflective tape) appear as three dark triangles on the IR image. The three blue arrows indicate the positioning of the three LDF probes.

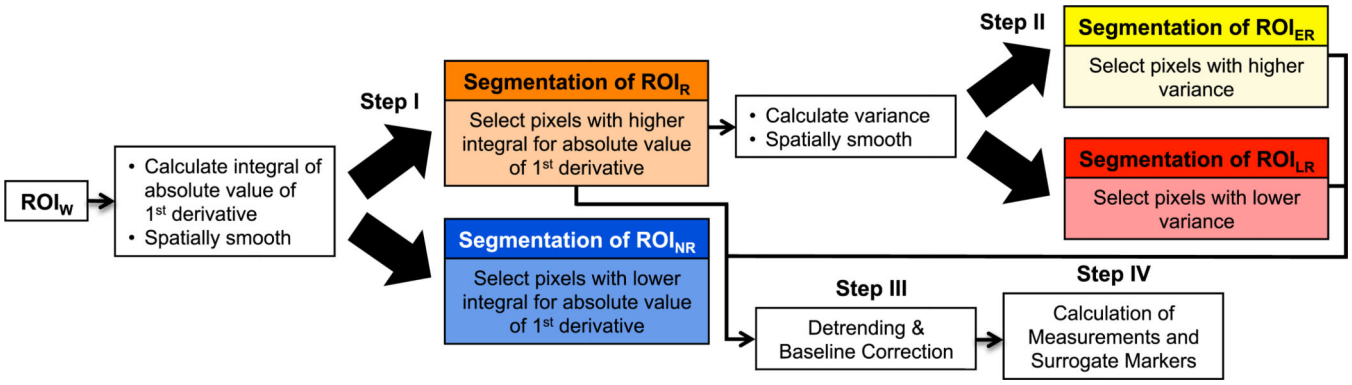

Figure 2.

Flow diagram of image processing for each subject: classification (Steps I and II), detrending and baseline correction (Step III), and temporal marker calculation (Step IV).

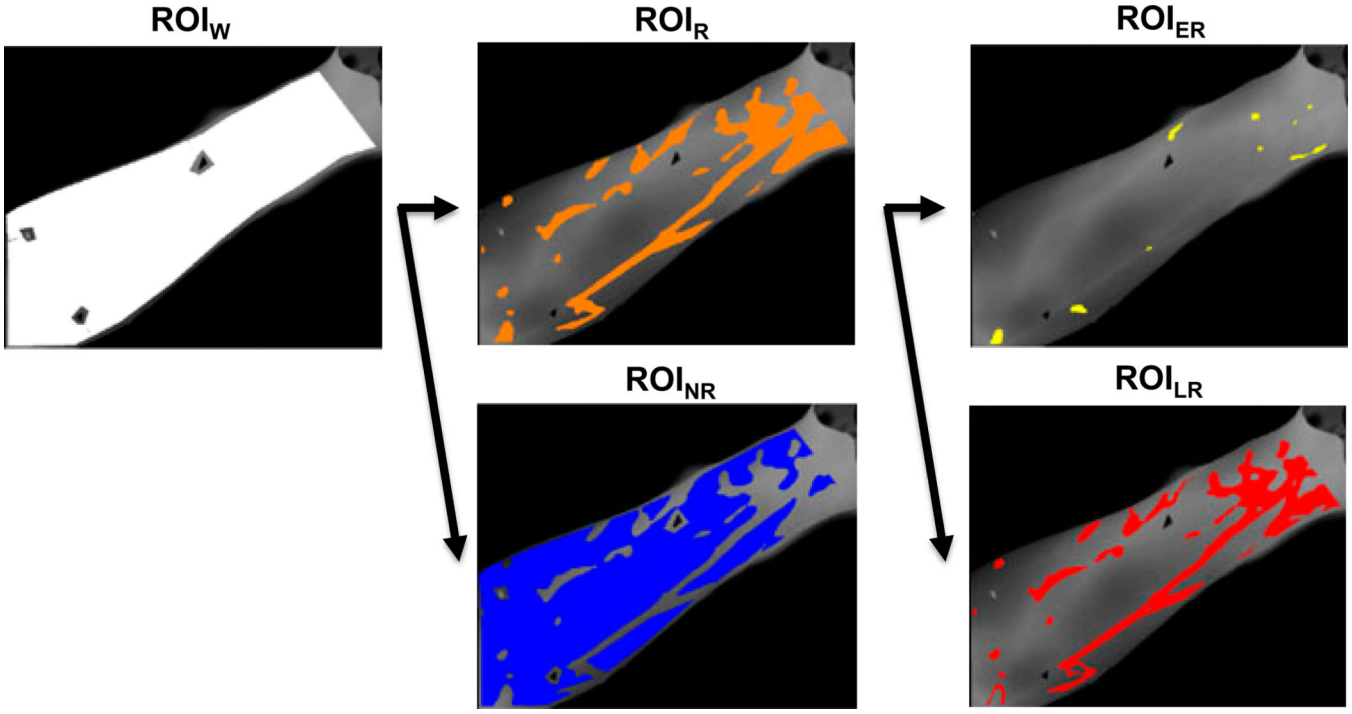

Figure 3.
Classification results of ROI$_R$, ROI$_{NR}$, ROI$_{ER}$, and ROI$_{LR}$ (Figure 2, Steps I and II) of a representative subject.

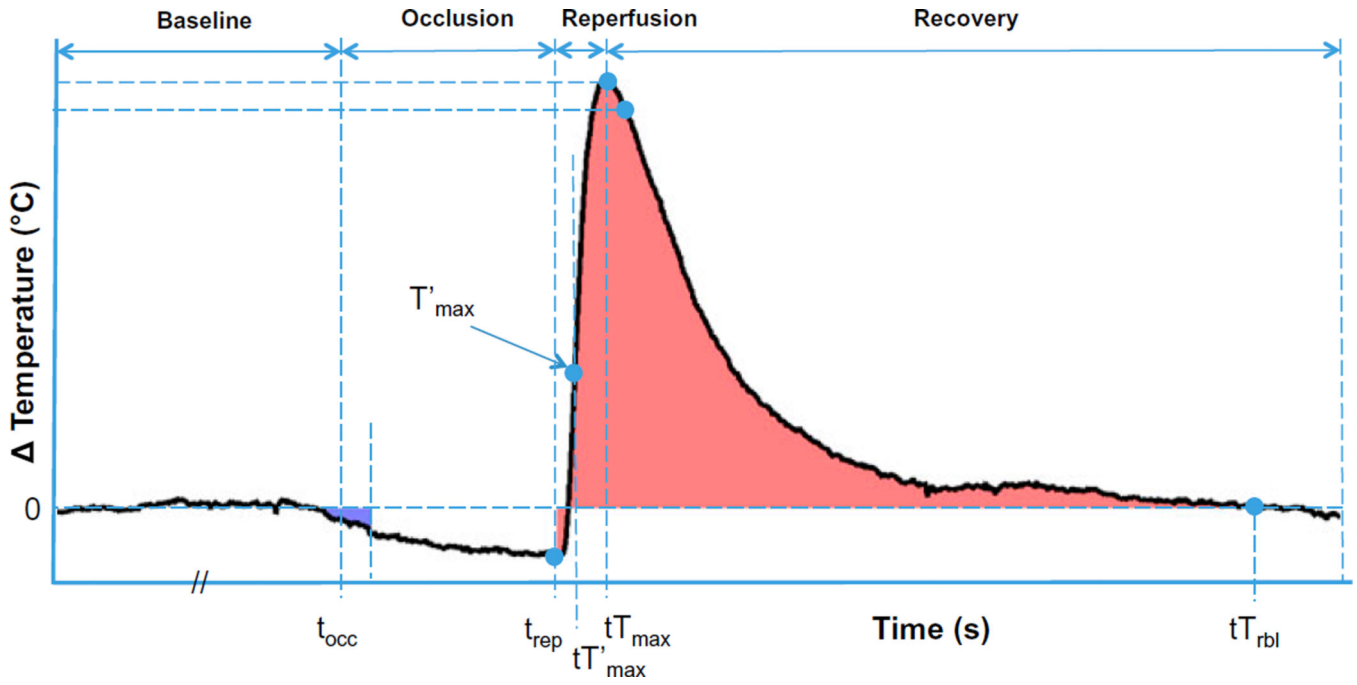

Figure 4.

Time–temperature profile (representative subject), following detrending and baseline correction steps, with segments of PORH test and measurements labelled.

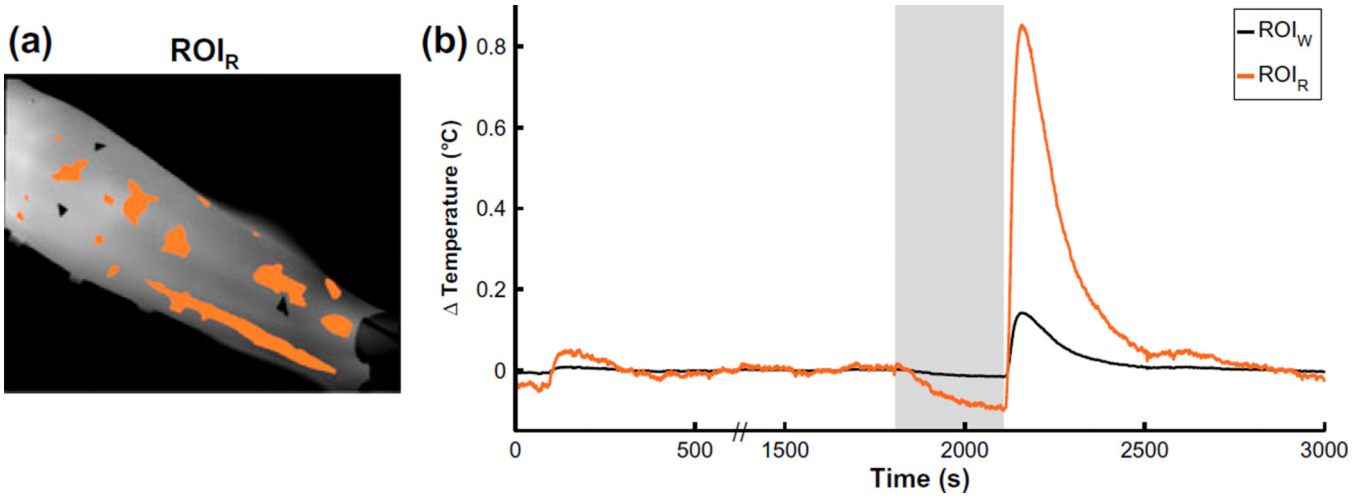

Figure 5.

(a) Computed ROI_R (clusters of orange pixels) overlying the raw IR image of a representative subject's forearm. (b) Time–temperature profiles of the ROI_W (black) and ROI_R (orange) from the same subject.

Notes: Both profiles are detrended and baseline-corrected to reflect changes in forearm temperature over time. The occlusion segment is highlighted in grey.

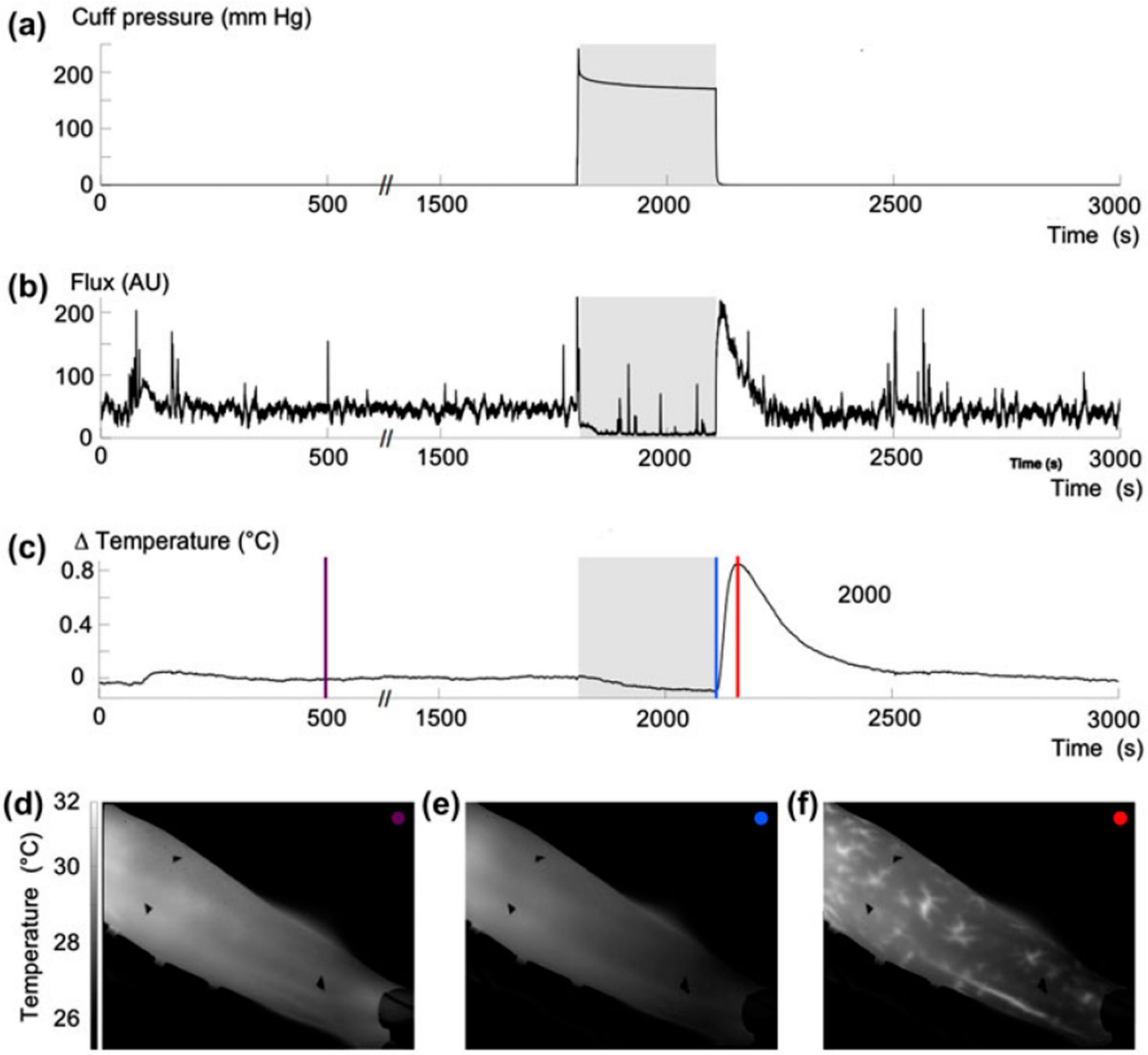

Figure 6.

(a) Cuff pressure vs. time (b) LDF flux vs. time, (c) ROI_R detrended, baseline-corrected temperature vs. time during PORH test from a representative subject. The occlusion segment is highlighted in grey. IR images of the volar aspect of forearm collected during (d) baseline, (e) occlusion, and (f) peak of reperfusion. Times of image collection are denoted as coloured vertical lines in (c) and corresponding coloured dots in (d), (e), and (f).

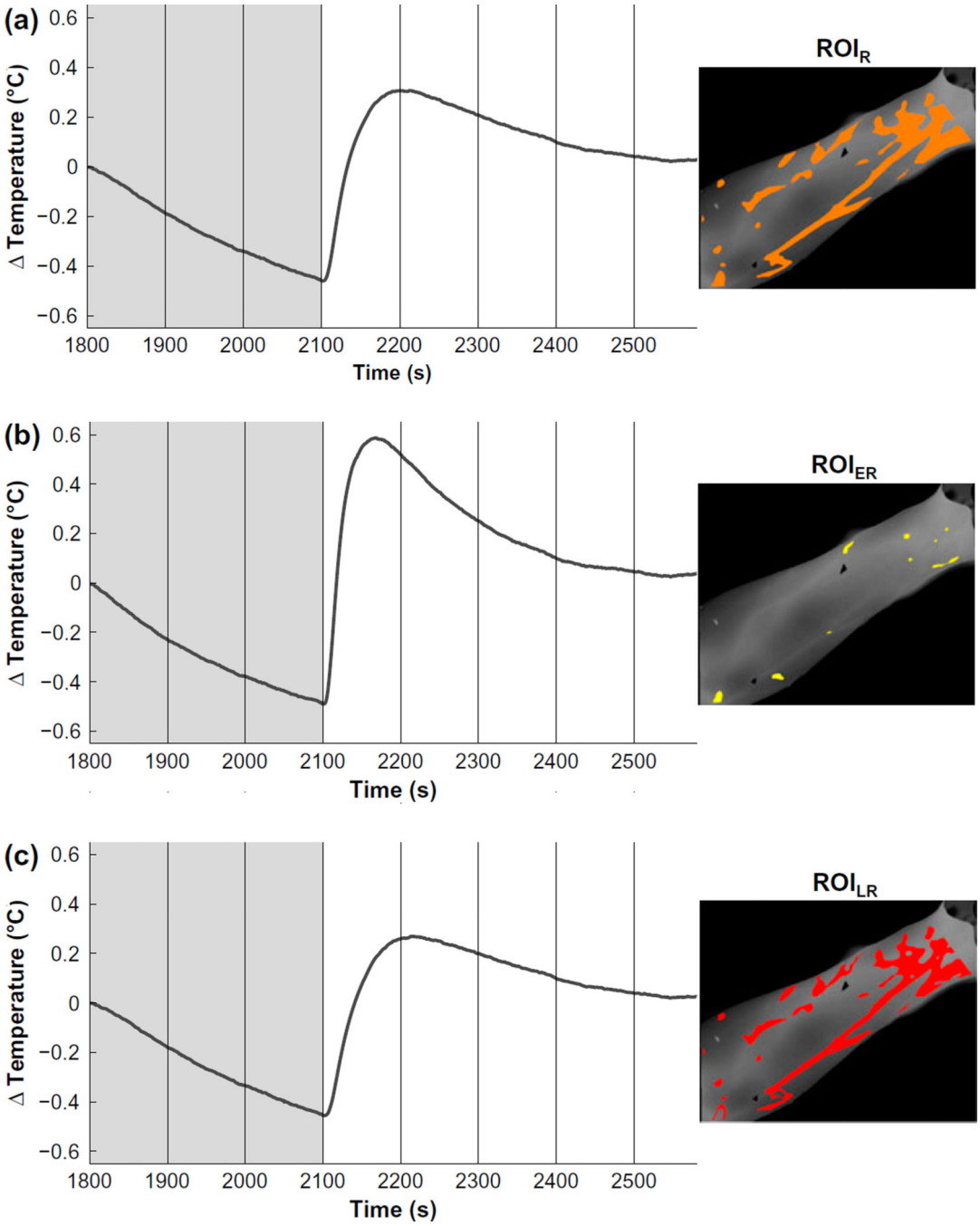

Figure 7.

The average change in temperature vs. time for (a) ROI_R, (b) ROI_{ER}, and (c) ROI_{LR} following detrending and baseline correction.

Notes: The occlusion time segment is highlighted in grey. Corresponding ROIs for a representative subject are shown on the right.

Table 1

Definition of derived measurements from the detrended, baseline-corrected time–temperature profiles.

Measurements	Definition
t_{occ}	Time point corresponding to the start of occlusion (s)
t_{rep}	Time point corresponding to start of reperfusion (s)
tT'_{max}	Time point corresponding to maximum temperature derivative during reperfusion (s)
tT_{max}	Time point corresponding to the peak perfusion (s)
tT_{rbl}	Time point at which temperature returns to baseline during recovery (s)
T'_{max}	Maximum temperature derivative during reperfusion (m °C/s)
T_{max}	Temperature corresponding to the peak of reperfusion (°C)
T_{30s}	Temperature corresponding to 30 s after peak of reperfusion (°C)

Note: m °C represents millidegree Celsius.

Table 2

Surrogate markers calculated from derived measurements.

Surrogate marker	Definition
ROI_R (% of ROI_W)	$ROI_R/ROI_W \times 100$
ROI_{ER} (% of ROI_W)	$ROI_{ER}/ROI_W \times 100$
ROI_{LR} (% of ROI_W)	$ROI_{LR}/ROI_W \times 100$
Baseline temperature (°C)	Mean temperature between (t_{occ} – 300 s) and t_{occ}
First 60 s Occlusion (°C × s)	$\int T(t)\,dt$ between t_{occ} and (t_{occ} + 60 s)
T_{max} (°C)	ΔT_{max} (relative to baseline-corrected)
T_{min} (°C)	ΔT_{min} (relative to baseline-corrected)
$\Delta t_{tT_{max}-t_{rep}}$ (s)	$tT_{max} - t_{rep}$
$\Delta t_{tT'_{max}-t_{rep}}$ (s)	$tT'_{max} - t_{rep}$
$\Delta t_{tT_{max}-tT'_{max}}$ (s)	$tT_{max} - tT'_{max}$
Slope (m °C/s)	Mean temperature derivative between t_{rep} and tT'_{max}
Reperfusion and recovery (°C × s)	$\int T(t)\,dt$ between t_{rep} and tT_{rbl}
First 30 s of recovery	$(T_{max} - T_{30s})/T_{max}$
Recovery time (s)	$tT_{rbl} - tT_{max}$

Notes: All temporal markers were calculated after detrending and baseline correction except for baseline temperature, which is the pre-processed temperature. First 60 s occlusion and reperfusion and recovery shaded in blue and red, respectively, in Figure 4.

Table 3

Calculated spatial surrogate markers.

Surrogate marker	Healthy volunteer (*n* = 34)
ROI_R (% of ROI_W)	15.2 (9.5, 20.4)
ROI_{ER} (% of ROI_W)	2 (1.2, 3.1)
ROI_{LR} (% of ROI_W)	11.9 (7.8, 16.2)

Note: Data presented as median (interquartile range).

Table 4

Calculated ROI_R, ROI_{ER}, and ROI_{LR} surrogate markers.

Surrogate marker	ROI_R	ROI_{ER}	ROI_{LR}
Baseline temperature (°C)	29.3 (27.7, 30.3)	29.1 (27.9, 30.4)	29.3 (27.7, 30.2)
First 60 s occlusion (°C × s)	−1702 (−4390, 196)	−3053 (−6388, −449)	−1549 (−3803, 666)
T_{max} (°C)	0.25 (0.137, 0.56)	0.669 (0.409, 0.845)	0.233 (0.096, 0.491)
T_{min} (°C)	−0.309 (−0.415, −0.153)	−0.301 (−0.521, −0.142)	−0.304 (−0.408, −0.165)
$\Delta t_{tT_{max}-t_{rep}}$ (s)	94 (78, 117)	51 (37, 73)	104 (87, 137)
$\Delta t_{tT'_{max}-t_{rep}}$ (s)	17 (15, 19)	13 (12, 16)	18 (15, 23)
$\Delta t_{tT_{max}-tT'_{max}}$ (s)	72 (57, 99)	40 (24, 56)	84 (67, 107)
Slope (m °C/s)	10.6 (8.3, 12.2)	22.1 (17, 32.2)	7.6 (6, 9.7)
Reperfusion and recovery (°C × s)	59.7 (16.7, 109.5)	86.6 (51, 147.4)	55.2 (5.2, 96.1)
First 30 s of recovery	0.119 (0.061, 0.202)	0.169 (0.129, 0.217)	0.107 (0.071, 0.168)
Recovery time (s)	364 (226, 530)	357 (258, 452)	365 (203, 518)

Note: Data presented as median (interquartile range).